Article

Experimental Validation on Tissue-Mimicking Phantoms of Millimeter-Wave Imaging for Breast Cancer Detection

Simona Di Meo * , **Giulia Matrone** and **Marco Pasian**

Department of Electrical, Computer and Biomedical Engineering, University of Pavia, Via Ferrata 5, 27100 Pavia, Italy; giulia.matrone@unipv.it (G.M.); marco.pasian@unipv.it (M.P.)
* Correspondence: simona.dimeo@unipv.it; Tel.: +39-0382-985223

Featured Application: The proposed millimeter-wave imaging system could be used as an alternative technique for early-stage breast cancer detection, significantly increasing survival chances.

Abstract: Breast cancer is one of the leading causes of cancer death among women; to decrease the death rate for this disease, early detection plays a key role. Recently, microwave imaging systems have been proposed as an alternative to the current techniques, but they suffer from poor resolution due to the low frequencies involved. In this paper, for the first time, an innovative millimeter-wave imaging system for early-stage breast cancer detection is proposed and experimentally verified on different breast phantoms. This has the potential to achieve superior resolution for breasts with a high volumetric percentage of adipose tissue, and the merit to overcome the common misconception that millimeter-waves cannot achieve useful penetration depths for biological applications. Three phantoms were prepared according to the dielectric properties of human breast *ex vivo* tissues in the frequency range [0.5–50] GHz. Two cylindrical inclusions made by water and gelatin or agar, mimicking dielectric properties of neoplastic tissues, were embedded in the phantom at different depths up to 3 cm. Two double ridge waveguides, with mono-modal frequency band equal to [18–40] GHz, were used to synthetize a linear array of 24 elements in 28 positions, acquiring signals with a Vector Network Analyzer. The images were reconstructed by applying the Delay and Sum algorithm to calibrated data. The feasibility of a new imaging system with a central working frequency of about 30 GHz is experimentally demonstrated for the first time, and a target detection capability up to 3 cm within the phantom is shown. The presented results pave the way for a possible use of millimeter-waves to image non-superficial neoplasms in the breast.

Keywords: breast cancer detection; early diagnosis; microwave imaging; millimeter-wave imaging; tissue-mimicking phantoms

1. Introduction

Breast cancer is the most diagnosed cancer among women worldwide, the second most common cancer overall, and the fifth most common cause of death for cancer in women [1]. However, the current imaging techniques allow to detect cancer in early stage, increasing the survival chance for the patient. Nevertheless, their disadvantages (e.g., exposition to ionizing radiation for x-ray mammography), are pushing for new complementary or supplementary techniques for breast cancer detection [2].

To this aim, the possibility of using microwaves has been largely investigated by several research groups worldwide, since microwave medical imaging systems represent a potential low-cost, low-risk, and easy-to-use alternative [3,4]. In addition, the technological progresses made in microelectronics, material sciences and integrated systems have rendered compact and relatively low-cost instrumentation available, further encouraging the research on this topic.

Generally, microwave medical imaging systems are based on the detection of the dielectric contrast between healthy and neoplastic tissues, and several experimental campaigns demonstrated that this contrast exists up to 50 GHz, especially when the volume percentage of adipose tissue is comparatively high [5–10].

Microwave imaging systems rely on tomographic or radar approaches. In both cases, several prototypes have been proposed over the past decade [11–17], and some of them reached a high level of maturity, being tested on up to 400 women in pre-clinical stage [11]. Most recent works on microwave imaging have been published in 2019 and 2020 [18–22].

However, the central working frequency of all these systems does not exceed 15 GHz. This, for radar systems, provides a good penetration depth for virtually all breasts, but resolutions are not always optimal for an early diagnosis, especially for breasts with a high fat content (hence, low dielectric permittivity, which in turn means a comparatively large wavelength). On the other hand, for tomographic approaches, which in principle could offer optimal resolution in breasts with a high fat content, problems like high computational costs, long processing times, and the non-univocal solution of a usually ill-posed inverse problem, leave the search for better solutions still open.

To address this problem, higher frequencies could be used, even if the high values for propagation losses within biological tissues have been historically considered as the main motivation for them being employed only in the biomedical imaging of shallower regions [23].

Nevertheless, the idea of using millimeter-wave (mm-wave) frequencies has been recently explored, aiming at a possible use on breasts with a high fat content, by working on the dielectric characterization of breast tissues, the fabrication of breast phantoms suited for mm-wave operations, and the validation of the working principle on simulated and preliminary setups [7–10,24–27].

In this work, for the first time, several experimental tests of a mm-wave imaging prototype on tissue-mimicking breast phantoms (with dielectric losses up to around 40 dB/cm) are shown, demonstrating the possibility to reach a penetration depth of several centimeters (up to 3 cm), while achieving a good resolution. In particular, the linear synthetic array prototype used for these tests was based on two double-ridge waveguides (with mono-modal working bandwidth from 18 GHz to 40 GHz) and two linear actuators to move the antennas in the desired positions, emulating an array of 24 radiators in 28 positions. Different types of breast phantoms with increasing values for dielectric losses were used as imaging scenario. After the calibration of the measured data, the Delay and Sum (DAS) algorithm was employed for image formation.

The paper is organized as follows. In Section 2, the experimental setup is described, together with both the complete procedure for system calibration and the characterization of the system Point Spread Function (PSF). In Section 3, the algorithm for image reconstruction is described. In Section 4, the imaging results are shown and discussed. Finally, some conclusions are given in Section 5.

2. Materials and Methods

2.1. Experimental Setup

Because of the high signal loss during propagation within biological tissues, the multi-static radar architecture was adopted for all measurements. With this approach, it is possible to improve the final signal-to-noise ratio of the system, since the signal backscattered by the geometry is collected $M(M-1)$ times, where M is the number of antennas within the array. In particular, each antenna in turn transmits, and all other $(M-1)$ antennas receive the signal backscattered from the target. This procedure is repeated M times, each time using a different transmitting antenna. The complete experimental setup consisted of:

- Two truncated double-ridge waveguides (PNR180) with cut-off frequency for the fundamental mode, TE10, of 15.12 GHz and mono-modal bandwidth of [18–40] GHz;

- A two-port PNA Network Analyzer (Keysight E8361C, [28]), working in the frequency range from 10 MHz to 67 GHz, used to generate the signals and to store the scattering parameters for each transmitting/receiving configuration;
- Two flexible coaxial cables with high performance, to connect the PNA to the two antennas;
- Four micro-step actuators (Zaber T-LSM200A) used both to support the antennas and to allow their movement in the intended positions for the generation of the synthetic linear array;
- A laptop to drive both the actuators and signal acquisition.

A picture of the complete experimental setup is shown in Figure 1. In all tests presented in this paper, only two actuators were moved, allowing for the creation of a synthetic linear array for 2-D imaging. The antennas were oriented toward the floor and several anechoic panels were used to mitigate external interferences; a polystyrene layer was used as air-like phantom support. In all phantoms used for the test of our prototype, the skin layer was not included, being out of the main scope of this paper, which is the experimental validation of the possibility to achieve significant penetration depths, even at mm-wave frequencies within realistic phantoms, allowing for the formation of a suitable image.
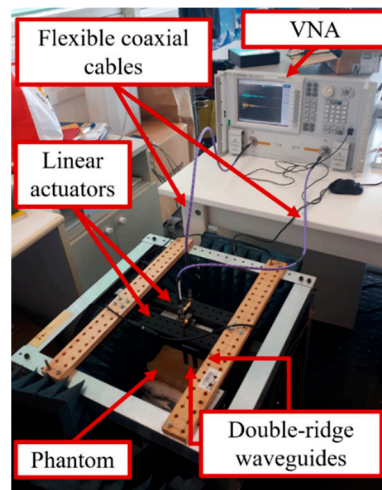

Figure 1. Experimental setup used for signal acquisition.

This is a simplifying hypothesis for what concerns the overall power budget, and the creation of multiple reflections within the propagation medium. However, on the one hand, the possibility of accounting for the skin losses as well, when adopting dedicated mm-wave transmit/receive modules, was already demonstrated [24]. On the other hand, possible strong multiple reflections (certainly increased by the skin, but at any rate created even by the sole presence of the air-fat interface of the phantoms used in this work, which intentionally does not use any coupling medium) can be largely addressed adopting image-formation algorithms more sophisticated than the DAS algorithm [29]. Therefore, this simplifying hypothesis is included to focus the attention on the main aspect (penetration depth at mm-wave frequencies), compensating for the sub-optimum power budget provided by a standard Vector Network Analyzer (VNA), and not confusing the results with more complex image-formation techniques, DAS being sufficient for the aim of this work, to compensate for the multiple reflections created by the air-fat interface. However, although due to the limitations of the standard VNA we used (especially its Noise Figure, NF), it was not possible to insert the skin layer or reduce the scanning time (about one hour, as explained below), the contribution of the skin was included in the theoretical calculation [24].

In addition, it should be noted that the final system, of which this prototype aims only to demonstrate the feasibility, will be composted both by dedicated transmit/receive

modules, with much lower NF (adding margin to consider the contribution of the skin too), as well as by a switch matrix connected to the physical antennas, which will significantly reduce scanning times.

In Figure 2, a sketch of the measurement scenario is represented. The Stepped Frequency Continuous Wave (SFCW) radar approach was used for data collection, and only transmission measurements were done (therefore, for each couple of antennas, only the S21 coefficient was measured). In the SFCW approach, each antenna-target-antenna combination is considered as a linear transfer function, with its behavior defined by means of its measured scattering matrix.
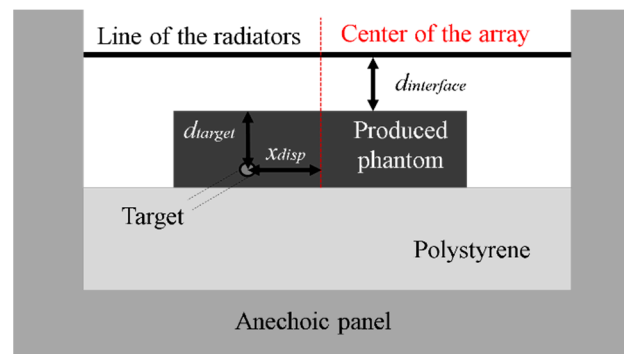
Figure 2. Sketch of the measurement scenario with the phantom, where d_{target} is the depth of the inclusion within the phantom, $d_{interface}$ is the distance of the phantom from the array, and x_{disp} is the lateral displacement of the target with respect to the center of the array.

The complete information on the target is derived by the amplitude and the phase of such transfer function between two antennas, and this information is used as input in the image reconstruction process, after the calibration procedure.

The synthetic array of 24 elements in 28 positions was achieved by linearly shifting the two antennas along a predetermined line with a phase center shift among adjacent radiators of 5 mm (i.e., half wavelength in air at 30 GHz), except for the physically adjacent antennas, for which the flange limited the spacing at 25 mm. The final width of the synthetic aperture was equal to 135 mm.

A MATLAB (The MathWorks, Natick, MA, USA) routine was used to coordinate both the signal acquisition and the antenna movement. The acquisition of each row of the scattering matrix was achieved as follows. Assume that at the beginning of the acquisition the transmitting antenna (#1) is in x_#1 = 0 mm, while the receiving antenna (#2) is in x_#2 = 25 mm. After the acquisition of the transmission parameter corresponding to this position, keeping the position of #1 fixed, #2 is shifted by 5 mm; therefore, we have x_#1 = 0 mm and x_#2 = 30 mm. This procedure is repeated until #2 reaches x_#2 = 135 mm. At this point, #1 (and consequently also #2) is shifted by 5 mm. So, for the acquisition of the whole second row of the scattering matrix we have x_#1 = 5 mm. Antenna #2, instead, is moved in linear steps of 5 mm from the initial position x_#2 = 30 mm to x_#2 = 135 mm. This procedure is repeated until antenna #1 reaches x_#1 = 110 mm.

Each time, only the transmission parameters (S21) were measured, and owing to the symmetry of the scattering matrix (reciprocal property of a passive network), it was not necessary to acquire each symmetrical transmission parameter, halving the acquisition time.

The antenna positions at each step are shown in Figure 3. Due to the physical dimension of the antenna support (flanges and other fixtures), the final synthetic array is not fully sampled, which turns out into several zeros in the complete scattering matrix. The relative transmit/receive apodization matrix is drawn in Figure 4; in this matrix, we indicated with 1 the cells that correspond to an active combination of transmit/receive antenna position, while 0 indicates that the transmit/receive event has not occurred (as an example, the element in Figure 4 cell (1,1) corresponds to x_#1 = 0 mm and x_#2 = 25 mm). The time

required by the antennas to cover the full active aperture and record all the data was about one hour per scan.

Figure 3. Schema of data acquisition. In this simplified schema realized for explanation purposes, 15 antenna positions are considered (instead of the 28 positions of the real array). Red and blue dots represent transmitting and receiving antennas, respectively.

												RX array																	
1	**2**	**3**	**4**	**5**	**6**	**7**	**8**	**9**	**10**	**11**	**12**	**13**	**14**	**15**	**16**	**17**	**18**	**19**	**20**	**21**	**22**	**23**	**24**	**25**	**26**	**27**	**28**		
0	0	0	0	0	1	1	1	1	1	1	1	1	1	1	1	1	1	1	1	1	1	1	1	1	1	1	1	**1**	
0	0	0	0	0	0	1	1	1	1	1	1	1	1	1	1	1	1	1	1	1	1	1	1	1	1	1	1	**2**	
0	0	0	0	0	0	1	1	1	1	1	1	1	1	1	1	1	1	1	1	1	1	1	1	1	1	1	1	**3**	
0	0	0	0	0	0	0	0	1	1	1	1	1	1	1	1	1	1	1	1	1	1	1	1	1	1	1	1	**4**	
0	0	0	0	0	0	0	0	0	1	1	1	1	1	1	1	1	1	1	1	1	1	1	1	1	1	1	1	**5**	
1	0	0	0	0	0	0	0	0	0	1	1	1	1	1	1	1	1	1	1	1	1	1	1	1	1	1	1	**6**	
1	1	0	0	0	0	0	0	0	0	0	1	1	1	1	1	1	1	1	1	1	1	1	1	1	1	1	1	**7**	
1	1	1	0	0	0	0	0	0	0	0	0	1	1	1	1	1	1	1	1	1	1	1	1	1	1	1	1	**8**	
1	1	1	1	0	0	0	0	0	0	0	0	0	1	1	1	1	1	1	1	1	1	1	1	1	1	1	1	**9**	
1	1	1	1	1	0	0	0	0	0	0	0	0	0	1	1	1	1	1	1	1	1	1	1	1	1	1	1	**10**	
1	1	1	1	1	1	0	0	0	0	0	0	0	0	0	1	1	1	1	1	1	1	1	1	1	1	1	1	**11**	*T*
1	1	1	1	1	1	1	0	0	0	0	0	0	0	0	0	1	1	1	1	1	1	1	1	1	1	1	1	**12**	*X*
1	1	1	1	1	1	1	1	0	0	0	0	0	0	0	0	0	1	1	1	1	1	1	1	1	1	1	1	**13**	
1	1	1	1	1	1	1	1	1	0	0	0	0	0	0	0	0	0	1	1	1	1	1	1	1	1	1	1	**14**	*a*
1	1	1	1	1	1	1	1	1	1	0	0	0	0	0	0	0	0	0	1	1	1	1	1	1	1	1	1	**15**	*r*
1	1	1	1	1	1	1	1	1	1	0	0	0	0	0	0	0	0	0	1	1	1	1	1	1	1	1	1	**16**	*r*
1	1	1	1	1	1	1	1	1	1	1	0	0	0	0	0	0	0	0	0	1	1	1	1	1	1	1	1	**17**	*a*
1	1	1	1	1	1	1	1	1	1	1	1	0	0	0	0	0	0	0	0	0	1	1	1	1	1	1	1	**18**	*y*
1	1	1	1	1	1	1	1	1	1	1	1	1	0	0	0	0	0	0	0	0	0	1	1	1	1	1	1	**19**	
1	1	1	1	1	1	1	1	1	1	1	1	1	1	0	0	0	0	0	0	0	0	0	1	1	1	1	1	**20**	
1	1	1	1	1	1	1	1	1	1	1	1	1	1	1	0	0	0	0	0	0	0	0	0	1	1	1	1	**21**	
1	1	1	1	1	1	1	1	1	1	1	1	1	1	1	1	0	0	0	0	0	0	0	0	0	1	1	1	**22**	
1	1	1	1	1	1	1	1	1	1	1	1	1	1	1	1	1	0	0	0	0	0	0	0	0	0	1	1	**23**	
1	1	1	1	1	1	1	1	1	1	1	1	1	1	1	1	1	1	0	0	0	0	0	0	0	0	0	0	**24**	
1	1	1	1	1	1	1	1	1	1	1	1	1	1	1	1	1	1	1	0	0	0	0	0	0	0	0	0	**25**	
1	1	1	1	1	1	1	1	1	1	1	1	1	1	1	1	1	1	1	1	0	0	0	0	0	0	0	0	**26**	
1	1	1	1	1	1	1	1	1	1	1	1	1	1	1	1	1	1	1	1	1	0	0	0	0	0	0	0	**27**	
1	1	1	1	1	1	1	1	1	1	1	1	1	1	1	1	1	1	1	1	1	1	0	0	0	0	0	0	**28**	

Figure 4. Transmit/receive apodization matrix.

2.2. System Calibration

Before using the received signals for image reconstruction, they must be properly calibrated. This operation is fundamental, since in this configuration the proximity between radiators provides very large mutual coupling, masking the contribution of all useful but very weak signals reflected by the illuminated scenario.

This unwanted signal is usually referred to as "crosstalk" and it is easily removed by subtracting the measurement done without the target to the one acquired with the target. In this way, both the antenna coupling and the environment multiple reflections are largely suppressed. In addition, since the imaging procedure makes use of both amplitude and phase information to reconstruct the final image, it is fundamental to properly calibrate the

phase of the received signal too. In fact, this is influenced by several factors (propagation in the waveguides, transitions, spurious backscattering, etc.). To this aim, a known calibration target is used, that is a metallic plate. This is a good standard, since its backscattering matrix is analytically known, and the corresponding phase delay is directly related to its distance from the antennas.

Therefore, according to [30], the complete calibration procedure is as follows. A first measurement (M_{plate}) with the metallic plate at a given distance in front of the array is done and the corresponding scattering matrix is calibrated by the crosstalk contribution (i.e., measurement with the plate minus measurement without the plate (M_{match})). The delay matrix corresponding to an ideal metallic plate at the same distance is analytically computed ($M_{analytics}$) [31]; the elements of this matrix are complex numbers given by $e^{-j2\pi f\tau}$, where f is the frequency and τ is the time delay. After this, the calibration of the whole imaging systems, made by cables, transitions and antennas is achieved by means of the ratio between these two matrixes. Then, the measurement of the target (M_{target}) calibrated by the crosstalk is multiplied by this correction matrix and the result is used in the image reconstruction procedure. The complete calibration procedure (M_{obj}) can be summarized by the following formula:

$$M_{obj} = \left(M_{target} - M_{match}\right)/\left(M_{plate} - M_{match}\right) \cdot M_{analytics} \tag{1}$$

This approach is valid in general and no further steps are required for target detection in air. On the other hand, for target detection within realistic breast phantoms, an additional step must be carried out. In this case, the calibration procedure must also consider the artifacts due to the strong reflection at the air-phantom interface. This contribution is generally very high and masks the following useful signal contribution that contains information about tumor presence. The use of a proper coupling medium could reduce it. However, due to the difficult maintenance of the system submerged in oil and problems related to the sterilization between repeated applications on different patients (in a potential clinical environment), as well as the impossibility of using the abovementioned calibration procedure with a coupling liquid, in this work, no coupling medium was employed.

To solve this problem, the time-gating approach is adopted; therefore, the image is reconstructed starting from the end of the interface reflection in time and space (therefore all the experimental images in phantoms do not start from z = 0 mm).

2.3. Simulated Point Spread Function

The PSF describes the response of an imaging system to a point source or to a point object, thus it can be seen as the impulse response of the system. From a practical point of view, the PSF gives a direct measure of the quality of an imaging system, being strictly related to the spatial resolution.

Two full-wave simulations (using the Ansys Electronics Desktop software) were done to determine the simulated PSF of the proposed mm-wave imaging system. Both the simulated full-wave models included 28 rectangular waveguides (working in the frequency range [26.5–40] GHz) in a linear configuration, in air (*Case 1*) and in a dielectric medium with the same dielectric properties of human breast *ex vivo* tissues (*Case 2*).

The antennas used in the simulated scenarios are common open ended WR28 waveguides. These have the same upper working frequency of the antennas used for the experimental setup (PNR180), but a higher lower working frequency (26.5 GHz instead of 18 GHz). Although this simulated setup works at frequencies not identical to those of the experimental setup, it is useful to provide an estimation of the PSF, while maintaining the computational effort within the limits of the available workstations (to deliver accurate, simulated, results for the image formation algorithm, the working bandwidth is discretized with a fine step of 50 MHz, and all points are calculated independently, thus the WR28 antennas are more convenient, to this aim, than PNR180 antennas). The distance between phase centers of adjacent radiators is equal to half wavelength at 30 GHz in each corre-

sponding medium. In both cases, the target was a sphere with the same average dielectric properties of human neoplastic tissues (ε'@30 GHz = 19 and ε''@30 GHz = 20, [8]), with a diameter of 2 mm (i.e., point-like, in accordance with the guidelines published in [32] for the evaluation of the PSF for a radar system), and placed at 4 cm depth from the center of the array. In these simulations, the final dimension of the array was 13.5 cm in air and 7.8 cm in fat.

The main-lobe width along the lateral and range directions of the simulated PSFs in both cases, i.e., in air and in fat, are summarized in Table 1, where also the comparison with the theoretical spatial resolution (computed according to [31,33]) is shown. In Figure 5a,b the DAS image for the simulations corresponding to *Case 1* and *Case 2* are shown, respectively. Results show that, in both cases, the theoretical and the simulated resolutions are comparable, considering that the formulas used to predict the theoretical values, while useful to provide an estimation, make use of assumptions that cannot be rigorously applied to the cases under analysis. First, the formulas are derived under far-field approximations, which is not the case, and the lateral resolution is determined according to the lateral dimension of the array, which is not immediately defined according to simple geometrical consideration because of the lossy medium and, again, the near-field propagation. In any case, the plane-wave approximation to derive the order of magnitude of the achieved resolution was used because it can greatly simplify the study of the problem and the interpretation of the results, without compromising the veracity of the analysis itself.

Table 1. Spatial Resolution Measured on the Simulated Point Spread Functions (PSFs) and Theoretical Values @ 33.25 GHz.

	Simulated *Range*-Resolution	Theoretical *Range*-Resolution	Simulated *Lateral*-Resolution	Theoretical *Lateral*-Resolution
Case 1	14.6 mm	14.3 mm	4.4 mm	2.7 mm
Case 2	10 mm	8 mm	3.4 mm	2.7 mm
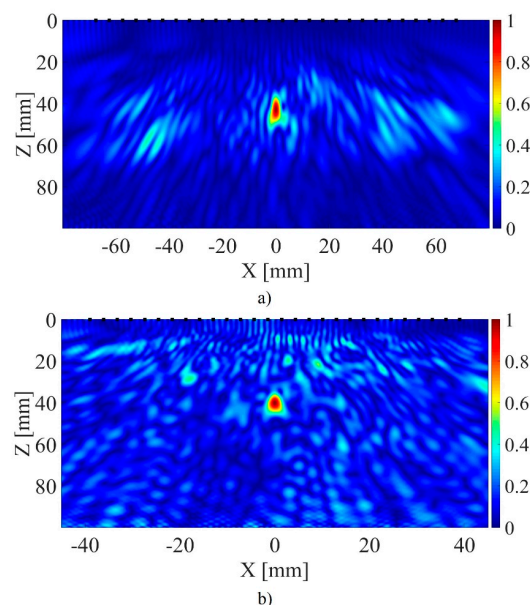
Figure 5. Simulated Point Spread Function for (**a**) *Case 1* and (**b**) *Case 2*.

2.4. Phantoms

According to the recipes proposed in [25,26] by our research group, different kinds of tissue-mimicking phantoms with increasing values of dielectric losses have been produced and used for the test of the mm-wave imaging system. In particular, three phantoms based

respectively on solidified oil (*Phantom1*), solidified Polysorbate 80 [26] (*Phantom2*), and oil-in-gelatin mixtures [25] (*Phantom3*) were used. The numbering of phantoms corresponds to the increasing values of dielectric properties, as well as to the logical and temporal progression of the performed tests. In Figure 6, a photo of the produced oil-in-gelatin phantom is shown. Details about the preparation of phantoms are omitted from this paper for brevity (being outside the scope of this work); however, interested researchers can find a detailed description of the recipes and procedures in [25,26]. In [25], the study of the reproducibility of the produced phantoms was presented.

Figure 6. Picture of the produced phantom (*Phantom3*) used for mm-wave imaging, in which the inclusion is visible.

On the same day of phantom preparation and imaging tests, the dielectric properties of the produced phantoms were also measured in order to avoid any alteration of results due to unwanted water evaporation. The dielectric properties were measured by means of an open-ended coaxial probe (Keysight 85070E Dielectric Probe Kit) in the frequency range [0.5–50] GHz, following the approach proposed in [25,26] to ensure both accurate and repeatable measurements, and they were compared to [8].

The targets embedded within the phantoms were made by water and gelatin or water and agar, in order to ensure a very significant dielectric contrast with the background phantom with a very fast and easy-to-produce mixture. The values of the real and imaginary part of the relative dielectric permittivity of the mixture made by water and gelatin at 30 GHz are 23 and 24.6, respectively; while, for the mixture made by water and agar at 30 GHz, they are 26.8 and 31.9, respectively. The comparison between the dielectric properties of *low-density* tissues (mean value $\pm$ one standard deviation) [8] and the ones of the produced phantoms in the frequency range [18–40] GHz is provided both for the real and imaginary parts of ε in Figure 7. In addition, the values for the dielectric permittivity of the three phantoms at 30 GHz are summarized in Table 2.
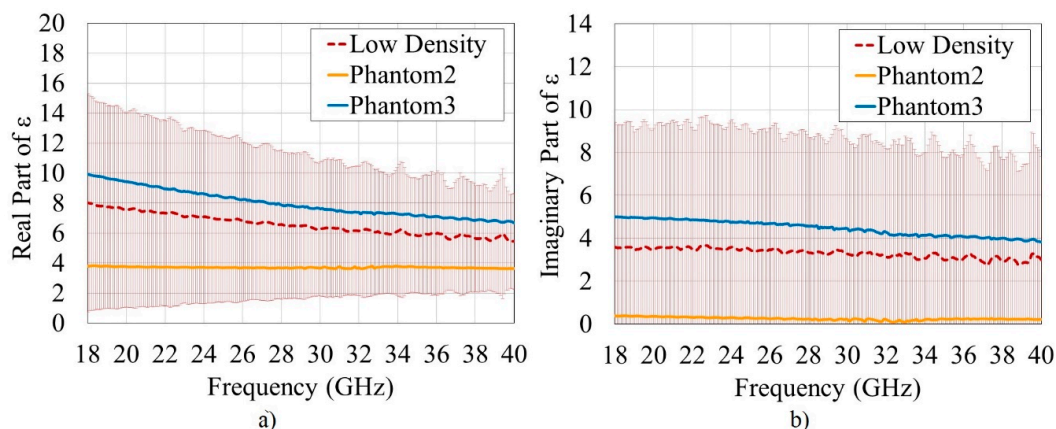
Figure 7. Comparison between the dielectric properties of the produced phantoms and the ones of the *Low density ex vivo* tissues [8] in the frequency range [18–40] GHz for the (**a**) real and (**b**) imaginary part of the dielectric permittivity.

Table 2. Dielectric Properties of the Produced Phantoms @ 30 GHz.

	ε'	ε''	α (dB/cm)
Phantom1	2.53	0	0
Phantom2	3.67	0.13	1.85
Phantom3	7.62	4.33	41.25
Low density ex vivo tissues [8], mean value	6.27	3.2	33.83

As may be noted, whereas for healthy tissues we did a categorization based on fat content, for tumor tissues we did not make any categorization. This was due to the physiological fact that tumor tissues are all characterized by increased blood supply and, therefore, higher water content. Our goal in this work was to demonstrate the possibility of detecting dielectric lesions up to a few centimeters in phantom with increasing values of attenuation (from zero to about 40 dB/cm). For these reasons, as well as because of the large variability of the tissues' dielectric properties, we produced simple mixtures composed only of water and gelatin to realize the dielectric inclusion, without focusing on the exact reproduction of the average dielectric properties of tumor tissues. The dielectric contrast (i.e., the difference between the dielectric properties of healthy and tumor tissues) we achieved was approximately 1:3 at 30 GHz when *Phantom3* for healthy and the mixture of water and gelatin for cancerous tissues are considered, and approximately 1:6 at 30 GHz when *Phantom2* and the mixture of water and gelatin are considered. In both cases, realistic values were achieved [7,8]. The target of our imaging system working in the mm-wave regime, indeed, is a breast with a high-volume percentage of fat tissue, i.e., with low values of ε.

From Figure 7, as well as from Table 2, it can be seen that the dielectric properties of *Phantom1* and *Phantom2* assume lower values than the average of human breast *low density ex vivo* tissues (i.e., lower signal attenuation values). Instead, for *Phantom3* the dielectric properties are slightly higher than the average of human breast *low density ex vivo* tissues. The final dimension of each phantom was about $23 \times 10 \times 5$ cm^3 (~800 mL). Due to the nature of phantoms, during imaging acquisitions, the temperature of the room was kept at ~20 °C to prevent the melting of the whole phantom.

3. Image Reconstruction

The image reconstruction process basically consists of two steps: the generation of backscattered signals from the measured and calibrated S21 coefficients, and DAS beamforming.

The S21 matrix was fed in input to a MATLAB routine that computed the radiofrequency (RF) signals received by each antenna after each transmission event (multi-static configuration with M antennas). To do so, a Gaussian pulse s_{TX} with a standard deviation $\sigma = 31$ ps, a central frequency $f_0 = 29$ GHz and a fractional bandwidth (measured at -6 dB) of ~60% was considered:

$$s_{TX}(t) = \cos(2\pi f_0(t - 4\sigma)) \exp\left(-(t - 4\sigma)^2/\sigma^2\right) \tag{2}$$

Such a signal was multiplied by each term of the scattering matrix S21 in the frequency (f) domain, to obtain the corresponding received signal s_{RX} after the application of the inverse Fourier transform, that is:

$$S_{RX\,i,j}(f) = F\{s_{TX}(t)\}S21_{i,j}(f) \tag{3}$$

$$s_{RX\,i,j}(t) = F^{-1}\{S_{RX\,i,j}(f)\} \tag{4}$$

where i and j represent the transmitting and receiving antenna, respectively, and F denotes the Fourier transform.

After that, synthetic focusing and DAS beamforming were implemented. The image was discretized in a set of 500×500 pixels, and for each pixel with coordinates (x, z) the time delay corresponding to the traveling path (τ) of the mm-wave from the transmitting

antenna in (x_i, z_i) to that image point and back to the receiving antenna in (x_j, z_j) was computed:

$$
\begin{aligned}
\tau_{i,j}(x,z) &= v^{-1}\big(\tau_i(x,z) + \tau_j(x,z)\big) \\
\tau_i(x,z) &= \sqrt{(x - x_i)^2 + (z - z_i)^2} \\
\tau_j(x,z) &= \sqrt{(x - x_j)^2 + (z - z_j)^2}
\end{aligned}
\tag{5}
$$

where v is the wave speed in the considered propagation medium. Subsequently, for each pixel, DAS beamforming was applied:

$$
I(x,z) = \sum_{i=1}^{M} \sum_{j=1}^{M} s_{RX\,i,j}\big(\tau_{i,j}(x,z)\big)
\tag{6}
$$

The final image was obtained by applying envelope detection to I, then squaring and finally normalizing the image, which was shown on a linear scale.

4. Results and Discussion

The mm-wave imaging prototype was first tested in air (Figure 8) and then on different kinds of phantoms with increasing values for dielectric losses (Figures 9–12), both including perfect scattering targets and more realistic ones, as previously summarized in Section 2.
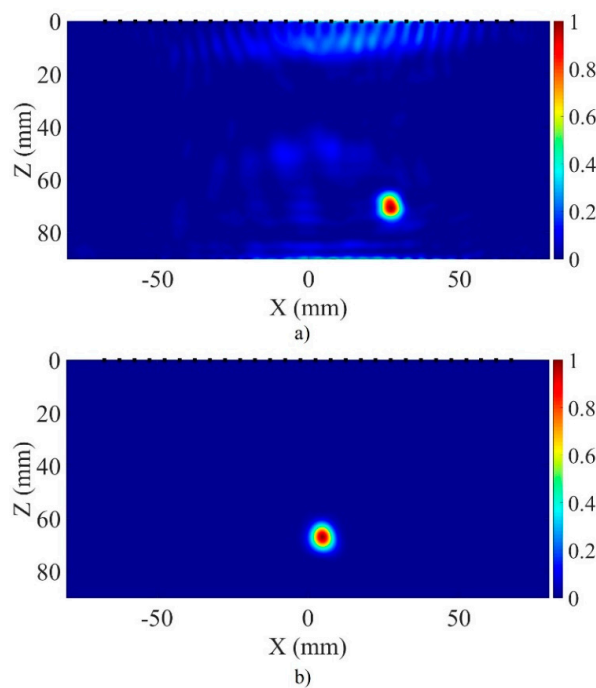
Figure 8. Reconstructed mm-wave image for (**a**) *Test 1* and (**b**) *Test 2*.
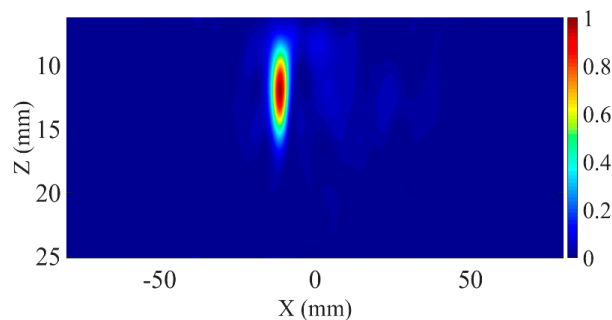
Figure 9. Reconstructed mm-wave image for *Test 3*.
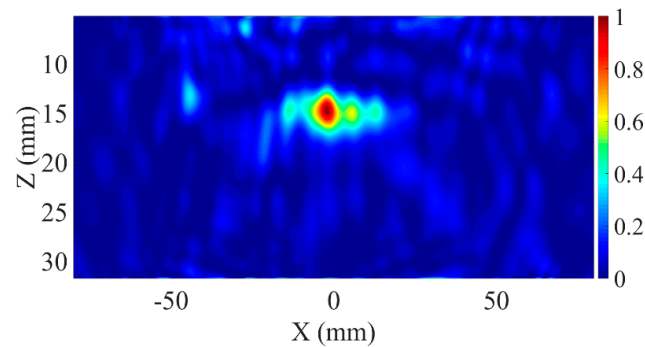
Figure 10. Reconstructed mm-wave image for *Test 4*.
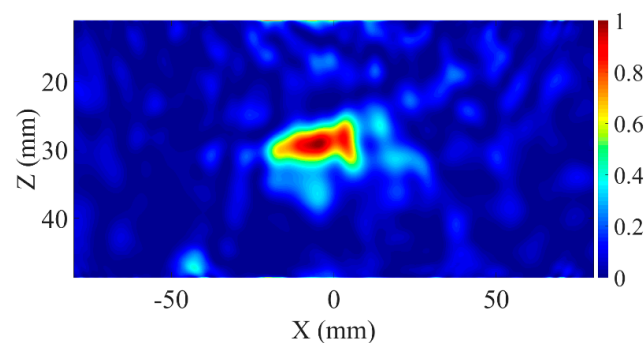
Figure 11. Reconstructed mm-wave image for *Test 5*.
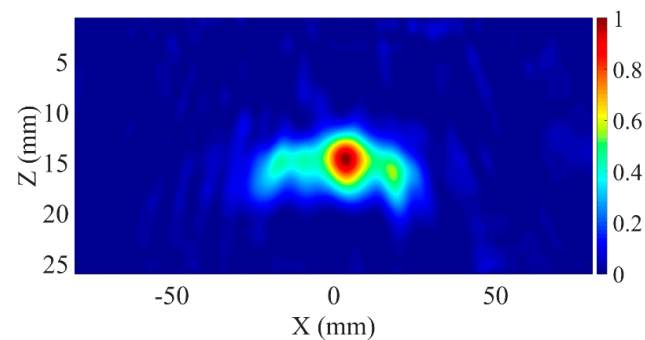
Figure 12. Reconstructed mm-wave image for *Test 6*.

Six cases will be presented in the following part of this paper. The first two tests are in air, both on a perfect scatterer (i.e., a metallic sphere, with 4 mm diameter, placed 7 cm ($d_{interface}$ = 7 cm) far from the center of the array and 3 cm laterally ($|x_{disp}|$ = 3 cm), (Test 1), and on a non-perfect scatterer, corresponding to a cylinder of deionized water and gelatin, with 8 mm diameter, placed 7 cm far from the center of the array in air and 0.5 cm laterally ($d_{interface}$ = 7 cm, $|x_{disp}|$ = 0.5 cm) (Test 2).

Subsequently, a different test involving the wave propagation in an almost lossless medium at 30 GHz is done on *Phantom1*. In this case (*Test 3*), the phantom top surface is 3 cm from the antenna array axis ($d_{interface}$ = 3 cm), and includes a cylinder made of deionized water and gelatin (diameter of 8 mm) at a depth of 1.2 cm (d_{target} = 1.2 cm). The lateral position of this target is about 1 cm ($|x_{disp}|$ = 1 cm) with respect to the center of the array.

Two further tests on tissue mimicking phantoms are then performed, this time using materials with non-zero dielectric losses, i.e., *Phantom2*. In both cases, the phantom included again a cylinder made by deionized water and gelatin or agar (diameter of 8 mm). First (*Test 4*), the *Phantom2* is placed 5 cm ($d_{interface}$ = 5 cm) from the antenna array, and the target inside it is at a 1.5 cm depth from the top surface (d_{target} = 1.5 cm). In the second case (*Test 5*),

Phantom2 is 2.5 cm from the synthetic antenna array ($d_{interface}$ = 2.5 cm) and the inclusion is placed at 3 cm depth (d_{target} = 3 cm).

The last test (*Test 6*) reported in this paper is done on a phantom with high dielectric losses (*Phantom3* in Figure 7). In this case, the 8 mm cylindrical inclusion is made of deionized water and agar. It is placed at a depth of 1.5 cm below the surface of the phantom (d_{target} = 1.5 cm), while laterally it is almost aligned to the center of the array. The phantom is placed 3.5 cm from the antennas ($d_{interface}$ = 3.5 cm).

In Table 3, a summary of the presented tests is shown. In all cases where the target is embedded into a phantom (i.e., not in air), the depth (*Z* axis) of the target shown in the following figures is computed considering the real propagation velocity of the signal in the phantom (which is equal to $v = 2\pi f / \beta$, where *f* is the frequency and β is the phase constant of the wave, computed by considering the dielectric properties of the phantom [34]).

Table 3. Summary of the presented tests.

Test	Medium	Target Materials (Diameter)	$d_{interface}$	$\lvert x_{disp} \rvert$	d_{target}
Test 1	Air	Metallic sphere (4 mm)	7 cm	3 cm	-
Test 2	Air	Water & Gelatine (8 mm)	7 cm	0.5 cm	-
Test 3	Phantom1	Water & Gelatine (8 mm)	3 cm	1 cm	1.2 cm
Test 4	Phantom2	Water & Gelatine (8 mm)	5 cm	-	1.5 cm
Test 5	Phantom2	Water & Gelatine (8 mm)	2.5 cm	-	3 cm
Test 6	Phantom3	Water & Agar (8 mm)	3.5 cm	-	1.5 cm

Therefore, calling d_{air} the equivalent distance in air of the target and $d_{interface}$ the distance between the phantom top surface and the axis of the synthetic antenna array (cf. Figure 2), the real depth of the target within the phantom (called d_{target}) is determined as:

$$(d_{air} - d_{\text{interface}})/c = (d_{\text{target}})/v \qquad (7)$$

The DAS images corresponding to the six case studies explained above are shown in the following pages. In particular, Figure 8a refers to *Test 1*, Figure 8b to *Test 2*, and Figures 9–12 to *Test 3–Test 6*.

As anticipated in Section 2, skin has not been considered in the tests reported in this paper, as this is the first experimental work on mm-wave imaging in tissue-mimicking phantoms; therefore, our primary objective was to demonstrate the ability to detect non-shallow targets within breast phantoms with increasing attenuation values using a system with a central working frequency of about 30 GHz. Although this simplifies the power budget and the effect of multiple reflections, does not imply a lack of validity. The extra loss given by the skin is calculated to be compensated for by dedicated transmit/receive modules [24]. Concerning multiple reflections, the setup intentionally avoids any coupling medium for the reasons explained in Section 2 (difficult maintenance/sterilization and calibration, aspects critical in a clinical perspective). This has the extra effect of generating multiple reflections even without the skin, which can be tackled by the DAS algorithm used in this work. Skin would no doubt increase multiple reflections, but these can be counter-acted for, at least partially, by using higher-order image-formation algorithms [29].

Comparing the two results in Figure 8a,b, it is evident that Figure 8a is more affected by side lobes than in case 8b, due to multiple reflections between the metallic target (used for Figure 8a) and the setup structure, which are instead absent in the case of the cylindrical gelatin inclusion (Figure 8b). The visible side lobes in each image, possibly due to the data acquisition procedure, could be reduced using more sophisticated beamforming algorithms. However, in this work we have chosen to use the basic DAS in order to compare the different test cases in the very same basic conditions and to evaluate system performance without adding further degrees of freedom in the image reconstruction process. It is also worth mentioning that an irregular shape of the target can be observed in Figure 11. However, this is due to a slight melting of the target during the inclusion procedure.

In addition, the multiple reflections presented in the image derived from measurements on *Phantom2* (Figures 10 and 11) are higher than those derived from measurements on *Phantom3* (Figure 12), index of a higher air bubble presence within *Phanton2* due to the fabrication procedure. By comparing Figures 10 and 12 another consideration could be done. In these two cases both the target dimension and composition are the same, as well as the target depth, which is almost 1.5 cm in both configurations. However, by comparing the resulting images, a bigger target can be seen in Figure 12 than in Figure 10. This result agrees with the theoretical expectation, because the signal attenuation in *Phanton3* is higher than the one in *Phantom2*; therefore, the effective array dimension in the case with highest dielectric losses is smaller, proving a worse resolution.

Concerning the diameter (8 mm) used for the water-gelatin inclusion, it should also be pointed out that this choice was determined by the fabrication procedure. Indeed, while offering great benefits such as low cost, safety, and ease of handling, out phantoms can only be modeled at high temperatures (before the solidification process takes place), and when the target mixture is injected in the background material [35] its high temperature causes a minimal melting of the background surrounding the inclusion. For this reason, in this work it was not possible to use cylinders with smaller diameters, although one of our next goals is to further modify the phantom fabrication procedure to overcome this limitation. Targets with a smaller diameter (2 mm) were in any case used for simulation analyses of the Point Spread Function presented in Section 2.3.

The distance between the radiator line and the phantom never exceeded a few cm; therefore, the phantom is in the near-field region of the antennas. Because of this proximity, the propagating electromagnetic wave is a spherical wave. This choice was based on the following considerations: on the one hand, in the final application the breast is expected to be in the vicinity of the antenna array (thus reasonably in the near-field region); on the other hand, moving the phantom farther from the antennas would have required a larger sample (along the lateral direction) due to the Half Power BeamWidth, becoming no longer compatible with the size of the standard phantom molds available in our laboratory.

Finally, let us clarify the aspects related to the resolution of microwave and mm-wave systems for imaging of highly adipose tissues. Let us suppose, for example, a simple case, i.e., a linear array of 14 cm size (please note that this is a fixed value that cannot be rescaled with frequency, it is imposed by the geometrical considerations about breasts) with a target placed 4 cm away from the center of the array surrounded by fat tissue, with very low dielectric permittivity values, which are constant for all the frequencies of interest ($\varepsilon' = 3$, $\varepsilon'' = 0.3$). This last assumption can be approximately correct only when low water content tissues, such as fatty ones, are considered.

Let us also suppose that between the fat tissue and the antenna array there is neither a matching layer nor an air layer, so 4 cm are entirely within fat. Under these hypotheses, we can make a comparison between the expected theoretical resolutions achievable by common microwave systems and our own.

If we consider, for example, two possible central working frequencies for a microwave imaging system of 5 GHz and 10 GHz, with bandwidths of 3 GHz and 6 GHz, respectively, the achievable range/lateral resolutions (computed by means of the formulas proposed in [31,33]) are 2.88 cm/9.89 mm and 1.44 cm/4.94 mm, respectively.

In our system, the central working frequency is 29 GHz with a 22 GHz band, so the expected theoretical range and lateral resolutions are 3.9 mm and 1.7 mm, respectively. Therefore, an improvement in terms of theoretical resolutions obtained when using higher frequencies in particularly fatty tissues is evident, which could allow an earlier diagnosis.

On the other hand, the main limitation of mm-waves in the biomedical field is the reduced penetration depth of the signal into tissues, due to the high values of attenuation during propagation. In this paper, we have shown that penetration depths in the order of a few centimeters are experimentally possible in tissue-mimicking breast phantoms and that our proposed system is able to correctly identify the target position in all the presented scenario. In particular, for *Phantom2*, with an attenuation slightly below 2 dB/cm,

a penetration of around 3 cm was achieved. It is worth noting that deeper penetrations are possible, provided that a thicker phantom can be realized. For *Phantom3*, with an attenuation slightly above 41 dB/cm, a penetration of around 1.5 cm was still possible, despite the sub-optimum hardware possibilities, most notably the use of a standard VNA instead of a dedicated transmit/receive module.

This performance (both in terms of penetration depth and scanning time) can undoubtedly be improved, through the use of dedicated transceivers and switch matrices, although it should be noted that penetration depths of a few centimeters are sufficient to entirely scan a flattened breast (derived from the woman supine position). In addition, it has been shown in [9] that about 40% of post-menopausal women included in the database [7,8] have a breast characterized by a high percentage of adipose tissue (with dielectric permittivity values between 2.6 and 4.9 for the real part and between 0 and 2.7 for the imaginary part), so it is realistic to assume particularly low dielectric permittivity values, making significant penetration depths possible also at mm-waves. In this regard, it is important to note that, since the proposed imaging technique is intended to be a screening system, the target population is not the whole female population (where the percentage of very fat breasts would not be high), but the one considered at risk (depending, among other factors, on age), where a higher percentage of fat breasts is expected.

5. Conclusions

In this paper, the first experimental tests of an innovative mm-wave imaging system for early-stage breast cancer detection were presented.

In particular, a synthetic linear array achieved by shifting two double-ridge waveguides, with mono-modal frequency band from 18 to 40 GHz, in 28 different positions was used and three different phantoms mimicking the dielectric properties of human breast fat tissues were considered as propagation media. The targets consisted of materials able to mimic the dielectric properties of human neoplastic tissues, and they were included from 1.2 cm to 3 cm depth within the phantom, demonstrating the good detection capability of the proposed system in all cases. In this work we demonstrated the feasibility of a millimeter wave imaging system, where dedicated transmit and receive modules, characterized by a lower Noise Figure (which would add further margin in terms of detectable signal), are supposed to be used. In addition, this envisaged future system will be based on a large number of physical antennas (e.g., 28). Although this is not going to modify the working principle with respect to the presented two-antennas scenario, it will improve significantly the scanning time, as in that case the different measurements are collected very rapidly using a switch matrix, instead of mechanically positioning the antennas. This will bring the system a step forward a real-life usability. Therefore, these promising results are certainly significantly below the limits that can be achieved with dedicated transmit/receive modules, conformal arrays, and advanced image-formation algorithms, they represent the first images of their kind in the field of mm-wave biomedical imaging.

Institutional Review Board Statement: Not applicable.

Informed Consent Statement: Not applicable.

Data Availability Statement: The data presented in this study are available on request from the corresponding author.

Conflicts of Interest: The authors declare no conflict of interest.

References

1. American Institute for Cancer Research. Available online: https://www.wcrf.org/dietandcancer/breast-cancer (accessed on 20 May 2020).
2. World Health Organization. Available online: https://www.who.int/cancer/detection/breastcancer/en/index1.html (accessed on 20 May 2020).
3. Nikolova, N.K. Microwave Imaging for Breast Cancer. *IEEE Microw. Mag.* **2011**, *12*, 78–94. [CrossRef]
4. O'Loughlin, D.; O'Halloran, M.J.; Moloney, B.M.; Glavin, M.; Jones, E.; Elahi, M.A. Microwave Breast Imaging: Clinical Advances and Remaining Challenges. *IEEE Trans. Biomed. Eng.* **2018**, *65*, 2580–2590. [CrossRef]
5. Lazebnik, M.; McCartney, L.; Popovic, D.; Watkins, C.B.; Lindstrom, M.J.; Harter, J.; Sewall, S.; Magliocco, A.; Booske, J.H.; Okoniewski, M.; et al. A large-scale study of the ultrawideband microwave dielectric properties of normal breast tissue obtained from reduction surgeries. *Phys. Med. Biol.* **2007**, *52*, 2637–2656. [CrossRef]
6. Lazebnik, M.; Popovic, D.; McCartney, L.; Watkins, C.B.; Lindstrom, M.J.; Harter, J.; Sewall, S.; Ogilvie, T.; Magliocco, A.; Breslin, T.M.; et al. A large-scale study of the ultrawideband microwave dielectric properties of normal, benign and malignant breast tissues obtained from cancer surgeries. *Phys. Med. Biol.* **2007**, *52*, 6093–6115. [CrossRef] [PubMed]
7. Martellosio, A.; Bellomi, M.; Pasian, M.; Bozzi, M.; Perregrini, L.; Mazzanti, A.; Svelto, F.; Summers, P.E.; Renne, G.; Preda, L. Dielectric Properties Characterization From 0.5 to 50 GHz of Breast Cancer Tissues. *IEEE Trans. Microw. Theory Tech.* **2017**, *65*, 998–1011. [CrossRef]
8. Di Meo, S.; Espin-Lopez, P.; Martellosio, A.; Pasian, M.; Bozzi, M.; Perregrini, L.; Mazzanti, A.; Svelto, F.; Summers, P.; Renne, G.; et al. Dielectric properties of breast tissues: Experimental results up to 50 GHz. In Proceedings of the 12th European Conference on Antennas and Propagation (EuCAP 2018), London, UK, 9–13 April 2018.
9. Di Meo, S.; Matrone, G.; Espin-Lopez, P.F.; Martellosio, A.; Pasian, M.; Bozzi, M.; Perregrini, L.; Mazzanti, A.; Svelto, F.; Summers, P.E.; et al. Correlation Between Dielectric Properties and Women Age for Breast Cancer Detection at 30 GHz. In Proceedings of the 2018 IEEE International Microwave Biomedical Conference (IMBioC), Philadelphia, PA, USA, 14–15 June 2018; pp. 190–192.
10. Summers, P.; Vingiani, A.; Di Pietro, S.; Martellosio, A.; Espin-Lopez, P.F.; Di Meo, S.; Pasian, M.; Ghitti, M.; Mangiacotti, M.; Sacchi, R.; et al. Towards mm-wave spectroscopy for dielectric characterization of breast surgical margins. *Breast* **2019**, *45*, 64–69. [CrossRef]
11. Grzegorczyk, T.M.; Meaney, P.M.; Kaufman, P.A.; Di Florio-Alexander, R.M.; Paulsen, K.D. Fast 3-D Tomographic Microwave Imaging for Breast Cancer Detection. *IEEE Trans. Med. Imaging* **2012**, *31*, 1584–1592. [CrossRef] [PubMed]
12. Burfeindt, M.J.; Shea, J.D.; Van Veen, B.D.; Hagness, S.C. Beamforming-Enhanced Inverse Scattering for Microwave Breast Imaging. *IEEE Trans. Antennas Propag.* **2014**, *62*, 5126–5132. [CrossRef]
13. Bahramiabarghouei, H.; Porter, E.; Santorelli, A.; Gosselin, B.; Popovic, M.; Rusch, L.A. Flexible 16 Antenna Array for Microwave Breast Cancer Detection. *IEEE Trans. Biomed. Eng.* **2015**, *62*, 2516–2525. [CrossRef]
14. Paulsen, K.; Poplack, S.; Li, D.; Fanning, M.; Meaney, P. A clinical prototype for active microwave imaging of the breast. *IEEE Trans. Microw. Theory Tech.* **2000**, *48*, 1841–1853. [CrossRef]
15. Klemm, M.; Craddock, I.J.; Leendertz, J.A.; Preece, A.; Benjamin, R. Radar-Based Breast Cancer Detection Using a Hemispherical Antenna Array—Experimental Results. *IEEE Trans. Antennas Propag.* **2009**, *57*, 1692–1704. [CrossRef]
16. Fear, E.C.; Bourqui, J.; Curtis, C.; Mew, D.; Docktor, B.; Romano, C. Microwave Breast Imaging With a Monostatic Radar-Based System: A Study of Application to Patients. *IEEE Trans. Microw. Theory Tech.* **2013**, *61*, 2119–2128. [CrossRef]
17. Porter, E.; Coates, M.; Popovic, M. An Early Clinical Study of Time-Domain Microwave Radar for Breast Health Monitoring. *IEEE Trans. Biomed. Eng.* **2016**, *63*, 530–539. [CrossRef] [PubMed]
18. Fasoula, A.; Duchesne, L.; Gil Cano, J.D.; Lawrence, P.; Robin, G.; Bernard, J.-G. On-Site Validation of a Microwave Breast Imaging System, before First Patient Study. *Diagnostics* **2018**, *8*, 53. [CrossRef]
19. Fasoula, A.; Duchesne, L.; Moloney, B.; Gil Cano, J.; Chenot, C.; Oliveira, B.; Bernard, J.-G.; Elwahab, S.A.; Kerin, M. Pilot patient study with the Wavelia Microwave Breast Imaging system for breast cancer detection: Clinical feasibility and identified technical challenges. In Proceedings of the 2020 14th European Conference on Antennas and Propagation (EuCAP), Copenhagen, Denmark, 15–20 March 2020; pp. 1–5.
20. Aldhaeebi, M.A.; Alzoubi, K.; Almoneef, T.S.; Bamatraf, S.M.; Attia, H.; Ramahi, O. Review of Microwaves Techniques for Breast Cancer Detection. *Sensors* **2020**, *20*, 2390. [CrossRef]
21. Bevacqua, M.; Palmeri, R.; Scapaticci, R. Multiresolution Virtual Experiments for Microwave Imaging of Complex Scenarios. *Electronics* **2019**, *8*, 153. [CrossRef]
22. Ambrosanio, M.; Kosmas, P.; Pascazio, V. A Multithreshold Iterative DBIM-Based Algorithm for the Imaging of Heterogeneous Breast Tissues. *IEEE Trans. Biomed. Eng.* **2019**, *66*, 509–520. [CrossRef] [PubMed]
23. Topfer, F.; Oberhammer, J. Millimeter-Wave Tissue Diagnosis: The Most Promising Fields for Medical Applications. *IEEE Microw. Mag.* **2015**, *16*, 97–113. [CrossRef]

24. Di Meo, S.; Svelto, F.; Summers, P.E.; Renne, G.; Preda, L.; Bellomi, M.; Espin-Lopez, P.F.; Martellosio, A.; Pasian, M.; Matrone, G.; et al. On the Feasibility of Breast Cancer Imaging Systems at Millimeter-Waves Frequencies. *IEEE Trans. Microw. Theory Tech.* **2017**, *65*, 1795–1806. [CrossRef]

25. Di Meo, S.; Pasotti, L.; Iliopoulos, I.; Pasian, M.; Ettorre, M.; Zhadobov, M.; Matrone, G. Tissue-mimicking materials for breast phantoms up to 50 GHz. *Phys. Med. Biol.* **2019**, *64*, 055006. [CrossRef]

26. Di Meo, S.; Iliopoulos, I.; Pasian, M.; Ettorre, M.; Pasotti, L.; Zhadobov, M.; Matrone, G. Tissue mimicking materials for breast phantoms using waste oil hardeners. In Proceedings of the IEEE 13th European Conference on Antennas and Propagation (EuCAP 2019), Krakow, Poland, 31 March–5 April 2019.

27. Di Meo, S.; Conforti, D.; Pasian, M.; Matrone, G. Preliminary experimental results for imaging at millimetre-wave frequencies in breast phantoms. In Proceedings of the IEEE European Microwave Conference in Central Europe (EuMCE 2019), Prague, Czech Republic, 13–15 May 2019.

28. Keysight E8361A/C PNA Network Analyzer, Technical Specifications, Keysight Technologies. 2014. Available online: https://www.keysight.com/en/pd-1000004621%3Aepsg%3Apro-pn-E8361A/pna-series?cc=RS&lc=eng (accessed on 4 January 2020).

29. Elahi, M.A.; O'Loughlin, D.; Lavoie, B.R.; Glavin, M.; Jones, E.; Fear, E.C.; O'Halloran, M. Evaluation of Image Reconstruction Algorithms for Confocal Microwave Imaging: Application to Patient Data. *Sensors* **2018**, *18*, 1678. [CrossRef] [PubMed]

30. Ahmed, S.S.; Schiessl, A.; Schmidt, L.-P. A Novel Fully Electronic Active Real-Time Imager Based on a Planar Multistatic Sparse Array. *IEEE Trans. Microw. Theory Tech.* **2011**, *59*, 3567–3576. [CrossRef]

31. Balanis, C.A. *Antenna Theory: Analysis and Design*; Wiley-Interscience: Hoboken, NJ, USA, 2005.

32. Amineh, R.K.; McCombe, J.J.; Khalatpour, A.; Nikolova, N.K. Microwave Holography Using Point-Spread Functions Measured With Calibration Objects. *IEEE Trans. Instrum. Meas.* **2015**, *64*, 403–417. [CrossRef]

33. *IEEE Standard for Radar Definitions*; IEEE Std 686TM-2017 (Revision of IEEE Std 686-2008); IEEE: New York, NY, USA, 2017.

34. Pozar, D.M. *Microwave Engineering*, 4th ed.; Wiley: Hoboken, NJ, USA, 2011.

35. Di Meo, S.; Pasotti, L.; Lashkevich, E.; Magenes, G.; Pasian, M.; Matrone, G. Combining Millimeter-Wave Imaging, Ultrasound and Elastography in a New Multimodal Approach for Breast Cancer Detection: Initial Experimental Results. In Proceedings of the 2020 42nd Annual International Conference of the IEEE Engineering in Medicine & Biology Society (EMBC), Montreal, QC, Canada, 20–24 July 2020.